Delineating Light Hydrocarbon Configuration in Source Rocks from NMR Relaxation Mechanism of Nano-Confined Fluids

Jin-Hong Chen[1,*], *Stacey* Althaus[1], *Chao* Liu[1], *Mohammed* Boudjatit[2]

[1]Aramco Americas: Aramco Research Center -Houston, TX US
[2]Saudi Aramco, Saudi Arabia

Abstract. Relaxation times are key parameters in the NMR study of formation rocks. However, understanding and interpretation of measured relaxation results in source rocks remain challenging due to the complexity and heterogeneity of both the matrix and the enclosed fluids in the formation. Protons in solid kerogen interact with each other through dipolar coupling and cannot be accurately defined by a simple relaxation process. The majority of hydrocarbon and water in unconventional source rocks are in the nanopores, which restrict the translational diffusion of the fluid molecules. The classic NMR relaxation theory by Bloembergen-Purcell-Pound (BPP theory) used to study fluid in rocks does not take this restriction into account. There is a need to re-examine the accuracy of BPP theory for NMR applications to nanoconfined fluid for unconventional source rocks.

In this paper, we examine and discuss the impact of the molecular motion on the observed NMR results for both the solid and liquid compositions in source rocks at low and high fields. Dipolar coupling of protons in solid kerogen is estimated and discussed first with a focus on its influence on the acquired NMR signal. A formal calculation of NMR dipolar cross-relaxation between nanoconfined fluids with the matrix solid is then presented by considering the effects of nanoconfinement on molecular translational diffusion to explain experimental data measured in a synthetic nanoporous material with uniform pore sizes. It was found, both theoretically and experimentally, the nanoconfinement leads to an increase in the intermolecular dipolar cross-relaxation rate by two orders of magnitude. Even with the large enhancement, the magnitude of the relaxation coupling between the nanoconfined fluids and the kerogen cannot explain the observed peaks with large T_1/T_2 ratio in 2D T_1-T_2 spectra suggested in literature. A new storage model for light hydrocarbon in the kerogen matrix is proposed from the NMR relaxation study.

1 Introduction

Measurement of NMR relaxation times has been the backbone of NMR applications in petroleum industry for conventional sandstone and carbonate formations [1-7]. It provides useful information including porosity, moveable or free fluids, irreducible or bound fluids, clay bound water, fluid typing, and permeability index etc [8-10].

Unconventional source rock shale reservoirs are fine-grained sedimentary rock with extremely low permeability, consisting of minerals intertwined with organic matter [11, 12]. The vast increase in oil and natural gas production globally over the past decade is mainly from these reservoirs with the application of hydraulic fracturing technology [13]. In source rock shales, the generally hydrophilic mineral matrix comprises carbonate, quartz, and clays. The largely hydrophobic organic matter is composed of kerogen and bitumen [14]. The pores in the source rocks are associated with both organic kerogen and the mineral matrix[12] and can differ in their wettability and capacity to store fluids. The hydrocarbons in source rock shale reservoirs were generated *in situ* over millions of years through thermogenic and biogenic processes [14, 15]. The resulting reservoir fluids consist of hydrocarbons of varying size and connate brine [16]. Interpretation of measured experimental results in unconventional source rocks are greatly challenged by aforementioned structural and compositional heterogeneity, complex pore networks with varying surface properties and interconnectivity, complicated reservoir fluid composition, and an ultra-small matrix permeability of the source rock shales. It is further challenged by the small but broad range distribution of pore sizes from sub-nanometer to a few micrometers in the shales [11, 17, 18].

NMR has been proven to be a very useful method in laboratory and subsurface measurements for porosity and fluid identification [19-23]. For NMR applications in unconventional source rocks, the T_1-T_2 2D spectrum has special importance and has been widely used [22, 24-37], because 1D T_2 spectra are crowded with severely overlapping peaks from different pore fluids due to the fact that all the pores are small. Generally, the T_2 values spread in a small range with the largest value often smaller than 100 ms.

2D T_1-T_2 spectra of source rocks typically include peaks or a section of peaks with large T_1/T_2 ratio [22, 24-34]. Large T_1/T_2 ratio of nuclear spins was usually observed in solid state samples [38]. However, in low field NMR the first data point is usually acquired about 100 μs after the last radiofrequency (*r.f.*) pulse, by which time the NMR signal from solid spins

has decayed to zero. As a result, only the fluid components in the source rock may be observed with low field NMR. The observed peaks with large T_1/T_2 ratio has been suggested to be the fluids in small nanopores that are coupled with the solid kerogen matrix by the intermolecular dipolar cross-relaxation so the fluids have NMR property similar to solid [39]. However, to explain the results, it requires an intermolecular dipolar cross-relaxation rate between the liquid and matrix solid of ~10^6 s^{-1}, which is extremely large considering that the relaxation rates from proton dipolar coupling are in the 1 s^{-1} scale for small molecules in liquid state.

The cross-relaxation rate from dipolar coupling is one of the most important parameters in NMR, providing internuclear distances that are used in determining structure and dynamics of small and large molecules in the liquid phase [38, 40-43]. Cross-relaxation rates are best measured using longitudinal magnetization with 2D Nuclear Overhauser Effect Spectroscopy (NOESY) experiments [44, 45] or 1D exchange-based experiments, for simple cases, especially for a two-spin system [46, 47]. The intermolecular dipolar relaxation between the fluid and kerogen in a source rock shale sample has never been measured before. The main reason may be that it is almost impossible to isolate it in the presence of many different NMR relaxation mechanisms in a complex and heterogeneous source rock sample.

Cross-relaxation is the time averaging effect of the dipolar coupled nuclei from rapid molecular motion. Both dipolar coupling and its time averaging are fundamentally important in NMR study of source rocks. They determine different aspects of experimental results from NMR measurement because nuclear spins in kerogen and in fluid are in very different states with different net effect from dipolar coupling. In this paper, we examine and quantify dipolar coupling and dipolar relaxation to delineate observed NMR results in unconventional source rocks.

2 Methods

2.1 Experiments and samples

Three types of NMR experiments are used in this study. **Fig. 1** shows the pulse sequences for data acquisition: a) single pulse to acquire Free-Induction-Decay (FID), b) CPMG sequence to acquire a series of spin-echo [48, 49] as illustrated by the green curve, c) Inversion-CPMG to acquire 2D T_1-T_2 spectrum, d) 2D NOESY, e) 1D selective NOE. In **Fig. 1**, narrow and wide rectangles represent 90° and 180° radiofrequency (*r.f.*) pulses as labelled. The subscripts represent the pulse phases of the first cycle with the phase for data acquisition at *x* direction. The full phase cycling for each pulse and data acquisition refer to [50]. The first pulse in e) is a selective 90° excitation pulse. T_w is the wating time between two successive scans and is normally about five times the longest T_1 in the materials. T_E is the echo time. T_{1D} is a delay with varying length according to the T_1 values in the sample. T_D is a short delay for the electronics to respond after an *r.f.* pulse before the first data point can be acquired which called pre-scan-delay. The length of T_D depends on the *r.f.* frequency or the magnetic field strength. It is 6.5 μs for our 500 MHz NMR and approximately 55 μs for our 12 MHz NMR instruments. τ_m is the mixing time in the NOESY.

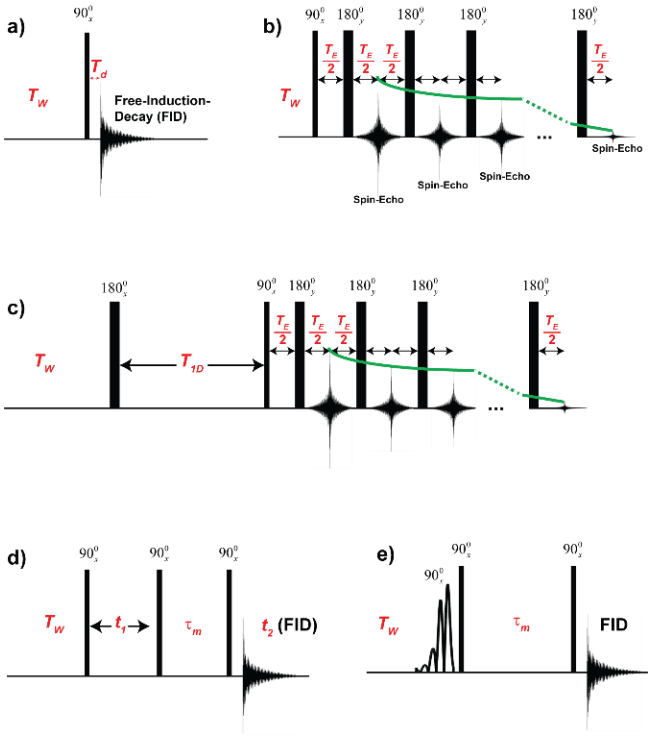

Fig. 1. NMR pulse sequences used in experiments. a) pulse sequence to acquired FID. b) CPMG echo pulse sequence. c) 2D T_1-T_2 pulse sequence. d) 2D NOESY sequence. e) 1D selective NOESY sequence. Rectangles represent *r.f.* pulse with the flip angles labeled on their top with number. The first pulse in e) is a selective 90° pulse. The subscripts of the *r.f.* pulses are their phase. Note that only the first cycle of all the pulses is labeled. The full phase-cycling for pulses and data acquisition (FID or Spin-Echo) can be found in [50] and for 1D selective NOE in [51].

2.1.1 Isolated kerogen and NMR measurement

Kerogen isolated from source rock using the same protocol as [52]. Only the float portion, with density smaller than 1.6 g/cm, was used in this study. This is to remove the majority of the pyrite in the sample; however, some small amount of pyrite and other paramagnetic minerals may remain in the isolated kerogen used in this study.

The isolated kerogen was dried at 110°C for 3 weeks. The residual fluid in the kerogen sample was measured at 12 MHz with an echo time of 110 μs using the CPMG measurement [49] and was found to contain 0.044 ml/g of the isolated kerogen.

The kerogen sample was then loaded into a 5 mm glass NMR tube for 500 MHz NMR experiments. An FID was acquired using a 90° excitation pulse with length 12 μs and Fourier transform to obtain a chemical shift NMR spectrum. Baseline spectrum with the empty NMR tube was also acquired at the same condition to make sure the acquired ^{1}H was from the kerogen sample.

^{1}H NMR spectrum of an isolated kerogen was also acquired using magic angle spinning (MAS) with a MAS rate of 5 kHz. The sample was packed in a 4 mm zirconia rotor. The FID was acquired using a single pulse on the 500 MHz spectrometer.

2.1.2 Source rock shale plug and 2D T_1-T_2 spectrum

Source rock plugs (1" diameter and 1" length) were saturated using Isopar at 8,000 psi for a week. The 2D T_1-T_2 NMR spectra were acquired using Inversion-Recovery-CPMG pulse sequence on a 12 MHz NMR (**Fig. 1**C) on a 12 MHz Oxford NMR instrument equipped with Green Imaging Technology (GIT) software. The general data acquisition parameters were: T_E = 110 μs, interscan delay T_w = 2.5 s, 30 different values of T_{1D} for the T_1 dimension, 64 scans were accumulated for each echo train. The acquired data was inverted using MUPen2D [53]. More details for NMR 2D T_1-T_2 of source rocks can be seen in reference [54].

2.1.3 Synthetic nanoporous materials and NMR measurements of intermolecular dipolar cross-relaxation rate

Methyl functionalized MCM-41 (MCM41-C1) with a pore diameter of 2.57 nm was purchased and used. Methanol-OD (CH_3OD, 98% atoms D, density ρ = 0.813 g/ml, molecular weight 33.05) was purchased and used without further purification. The MCM41-C1 was dried under vacuum at 50°C for one week. Saturation of the nanopores in MCM41-C1 was done based on capillary condensation [55, 56]. This method allows all the nanopores to saturate while leaving no observable fluids between the particles. The sample was then packed into a 4-mm magic-angle-spinning (MAS) NMR rotor for NMR measurement.

All the experiments were done at 22°C with a magic angle spinning (MAS) rate of 8000 Hz on a 500 MHz NMR spectrometer. The 2D NOESY [44, 45] were acquired using a mixing time (τ_m) of 800 ms. The selective NOE spectra were acquired using a 5 ms E-BURP-2 [57] and was on-resonance of the methanol methyl proton. More experimental details can be found in reference [58].

2.2 Dipolar coupling and time averaging in NMR

2.2.1 Dipolar coupling of nuclear spins

Dipolar coupling exists between any two nuclei with spin number ½. Here we only discuss proton or ^{1}H spins. Dipolar coupling of two protons $\vec{I}_i$ and $\vec{I}_j$ as shown **Fig. 2**a, best expressed by the interaction Hamiltonian, H_{DD}^{ij}, as

$$H_{DD}^{ij} = d_{ij}[\vec{I}_i \cdot \vec{I}_j - 3(\vec{I}_i \cdot \vec{e}_{ij})(\vec{I}_j \cdot \vec{e}_{ij})] \quad (1)$$

with $d_{ij} = (\mu_0 / 4\pi)\hbar\gamma_H^2 / r_{ij}^3$ the dipolar coupling constant, μ_0 = $4\pi\times10^{-7}$ N/A^2 the magnetic permeability in vacuum, γ_H = 2.675×10^8 rad·s/T the proton gyromagnetic ratio, $\hbar$ = 1.05×10^{-34} J·s Plank's constant, and r_{ij} the distance between the two protons, as illustrated in **Fig. 2**a.

Atoms in a molecule are on the time scale of ps to fs for vibration [59]. As a result, the only important term of the homonuclear dipolar coupling in NMR is the secular part of Eq. (1), as [38]

$$H_{DD}^{ij}(\theta_{ij}) = d_{ij}\frac{3\cos\theta_{ij} - 1}{2}(\vec{I}_i \cdot \vec{I}_j - 3I_{iz}I_{jz}) \quad (2)$$

where θ_{ij} angle between the two protons and the static field as shown in **Fig. 2**a.

The magnitude of dipolar coupling in frequency unit is $d_{ij} / 2\pi = 120$ kHz for two protons separated by a distance of $r_{ij} = 1.0$ Å. In an crystalline solid powder the two proton can be at any relative position and the resulted NMR spectrum is the dipolar Pake powder pattern [60], as plotted in **Fig. 2**b. Pake powder patterns can only be observed in specifically prepared crystalline samples [60, 61]. The spectral shape of many solid samples, however, does not follow the ideal Pake pattern. A main reason is that the studied materials are generally composed of many pairs of protons with different dipolar coupling constants. Instead, the NMR line-shape in these solids with complex dipolar broadening is often close to Gaussian shape and is best analyzed using the method of moments of the resonance curve [38, 62].

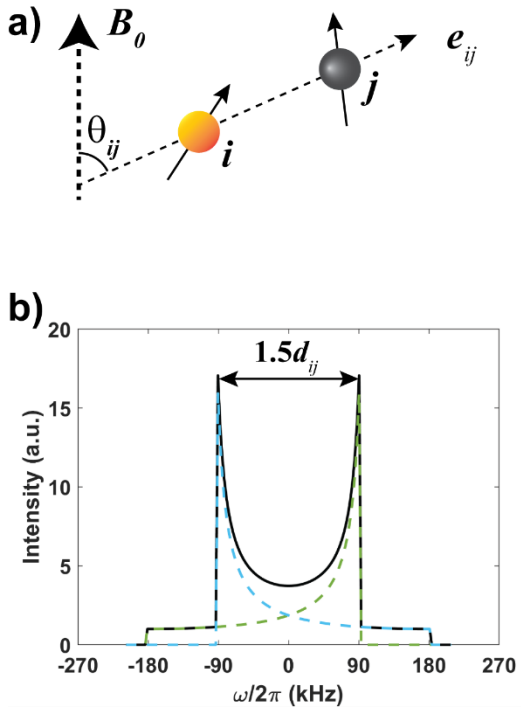

Fig. 2. a), schematic illustration of two protons $\vec{I}_i$ and $\vec{I}_j$ in space. b), the corresponding NMR spectrum of Pake pattern from dipolar coupling. B_0 and $\boldsymbol{e}_{ij}$ shows the direction of static magnetic field and unit vector, respectively. The plotted Pake pattern in (b) is calculated using a dipolar coupling constant d_{ij} = 120 kHz.

2.2.2 Time average of dipolar coupling from motion

The two protons in **Fig. 2**a can be from one molecule or on two different molecules. In non-rigid samples, the dipolar coupling undergoes modulation by the rapid random molecular motions, including rotational tumbling of individual molecules and relative translational motion of molecules, as illustrated in **Fig. 3** where spins *i* and *j* are on the same molecule and *j* and *k* are on different molecules. The molecular rotational tumbling modulates the dipolar coupling between spins *i* and *j* while translational motion modulates the dipolar coupling between spin *j* and *k*. Note that both the rotational and translational motions considered here are random diffusion [38]. In some cases, they are isotropic with equal opportunity in all the directions. In some other cases, these motion are anisotropic with preferential orientation [38, 59].

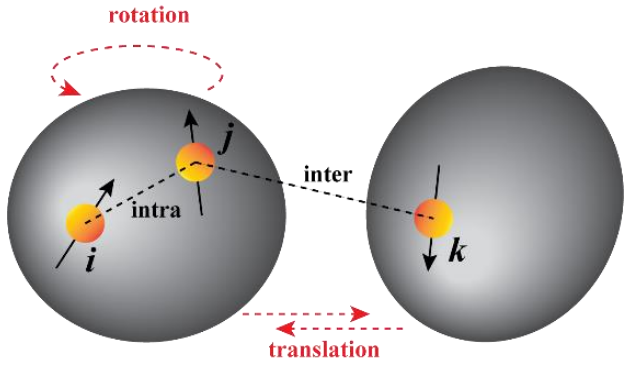

Fig. 3. Illustration of molecular rotation and translation and their effects on intramolecular and intermolecular dipolar coupling.

As a result of the molecular motion, the observed dipolar coupling is an average over a characteristic time τ, as

$$\overline{H_{dd}} = \tau^{-1}\int_0^{\tau} H_{dd}(\theta_{ij}(t), r_{ij}(t))dt \qquad (3)$$

For intramolecular dipolar coupling, r_{ij} is time-independent constant and θ_{jk} is time-dependant in Eq. (3). For intermolecular dipolar coupling, both θ_{jk} and r_{jk} are time dependent. The effects of molecular motion on dipolar coupling depend on a characteristic time constant τ which has been thoroughly studied and discussed [38, 43, 59, 63]. Here we only examine some simple aspects related to this study.

For NMR, one timescale is important: Larmor timescale τ_0 which relates to the Larmor frequency of the NMR static field ω_0 in frequency unit ($\omega_0 = 2\pi\gamma_H B_0$ where the B_0 is the static magnetic field) as

$$\omega_0\tau_0 \sim 1 \qquad (4)$$

The Larmor time τ_0 is inversely proportional to the magnetic field. **The appropriate** consideration of NMR interactions, such as dipolar coupling, depend on the relative scale of motion time constant τ with respect to Larmor time τ_0. At time scale $\tau \sim \tau_0$, the effect is quite complicated and will not be discussed further here. When $\tau >> \tau_0$, the molecular motions reduce the net dipolar coupling to a smaller value, which can be observed in different solids, such as dry kerogen, in which molecules have certain degree of mobility. When $\tau < \tau_0$, the average dipolar coupling is usually very small.

Table *1* lists some typical magnetic fields of NMR spectrometers used and the corresponding Larmor time.

The appropriate consideration of NMR interactions, such as dipolar coupling, depend on the relative scale of motion time constant τ with respect to Larmor time τ_0. At time scale $\tau \sim \tau_0$, the effect is quite complicated and will not be discussed further here. When $\tau >> \tau_0$, the molecular motions reduce the net dipolar coupling to a smaller value, which can be observed in different solids, such as dry kerogen, in which molecules have certain degree of mobility. When $\tau < \tau_0$, the average dipolar coupling is usually very small.

Table 1. Larmor time scale at different NMR field

$\omega_0/2\pi$ (MHz)	500	12	2
τ_0 (ns)	0.3	9.9	79.6

For small molecules in liquid and/or gas phases, the random molecular rotation and translation is always at time scale $\tau << \tau_0$, we have

$$\overline{H_{dd}} \approx 0 \qquad (5)$$

The net result of the dipolar coupling is then a pure relaxation mechanism and the resulted spectrum in frequency domain is in Lorentz shape [38, 43] with the width determined by the transverse relaxation time T_2. However, the heterogeneity of the magnetic field B_0 also contributes to the linewidth. For an NMR spectrum in Lorentzian shape, the full width at half height $\Delta\nu$ is determined as

$$\pi\Delta\nu = 1/T_2 + 1/T_2^{B_0} \qquad (6)$$

where T_2 and $T_2^{B_0}$ are the transverse relaxation time of the spins and a phenomenon relaxation time from heterogeneity of the NMR magnetic field B_0, respectively. Bulk susceptibility effect generated by paramagnetic minerals, which can be abundant in source rocks, can also contribute to magnetic field heterogeneity and influence the linewidth [64].

MAS was developed to remove the line-broadening generated by homogeneous interaction such as heteronuclear dipolar coupling and bulk susceptibility effect and reduce line-broadening of inhomogeneous interaction such as homonuclear dipolar coupling [64, 65]. Therefore, MAS NMR spectrum of solid can still include line-broadening from ^{1}H-^{1}H dipolar coupling but do not have bulk susceptibility effects from paramagnetic electron spins. For liquid and gas of small molecules, even in the pores, because of rapid molecular rotation and translation diffusion, the linewidth of MAS NMR spectrum is completely determined by relaxation times.

3 Results and discussion

3.1 Dipolar coupling in kerogen solid

Shown in **Fig. 4**a is the ^{1}H chemical shift spectrum of a dried kerogen sample, isolated from a source rock shale and shown as inset, acquired on 500 MHz spectrometer. The spectrum is the Fourier transform of the acquired FID as shown in **Fig. 1**a. For the 500 MHz spectrometer, the first data point of FID was acquired 6.5 μs after the 90° pulse. This allows the instrument to acquire ^{1}H NMR spectrum with large dipolar coupling or extremely short transverse relaxation.

Fig. 4b is the decomposition of the spectrum 4a using a Lorentzian (red curve) and a Gaussian (blue curve) line-shapes, representing protons from the remaining fluids and kerogen, respectively, as discussed in 2.2.1. The black and dashed green curves are the acquired spectrum 4a and summation of the Lorentzian and Gaussian spectra, respectively. The decomposition was done using 'fit' function in Matlab.

From the decomposition, the linewidth at half height of the Lorentzian and Gaussian spectra are 2.7 kHz and 13.8 kHz, respectively. The Lorentzian spectrum represents the remaining fluid in the kerogen sample. According to Eq. (6), the linewidth of the Lorentzian spectrum is determined by the summation of the relaxation time and the heterogeneity of the magnetic field, which is mainly from the susceptibility effect in the sample [38]. The fact that a single Lorentzian spectrum can effectively fit all the remaining fluids in different pores and environments suggests the primary factor determining its linewidth is the field inhomogeneity, i.e., susceptibility effect imposed by paramagnetic and/or ferromagnetic residuals in the kerogen sample. Therefore, 2.7 kHz gives the upper limit on the susceptibility effect in this sample at the 500 MHz.

For protons in kerogen, the linewidth of 13.8 kHz is much larger than 2.7 kHz. Therefore, this linewidth is dominated by the dipolar coupling. The $\Delta\nu$ = 13.8 kHz is much smaller than the estimated dipolar coupling of 120 kHz for two protons separated by 1 Å. The reasons are (i) the distance of protons in kerogen is much larger than 1 Å and more importantly (ii) there is certain degree of molecular motion in the solid kerogen.

Although a true T_2 cannot be accurately defined for a Gaussian shape, we use an equivalent $T_2^{eq} \sim 1/\pi\Delta\nu$ =23.1 μs to estimate when the NMR signal decays to zero. Since dipolar coupling is field independent, this value remains the same at all fields. At low field NMR, commonly used in oil/gas industry, the data are acquired with a CPMG pulse sequence, as shown in **Fig. 1**b. The first data point was acquired at about 100 μs. At this time, the hydrogen signal from solid kerogen decays to a negligible value. Therefore, the detected signals are only from fluids with sufficient rapid molecular motion. If the solid kerogen needs to be acquired, the first data point must be collected earlier than 23.1 μs and the length of the 90° excitation pulse should be as short as possible.

In **Fig. 4**c, we also showed the ^{1}H MAS NMR spectrum on an isolated kerogen with a MAS rate 5 kHz. The spectrum includes one single peak in Lorentzian shape and a few spinning sidebands. The linewidth at half height of the main peak is 810 Hz which corresponds to a T_2 of ~400 μs. Comparing to spectra a), the relatively small linewidth indicated that 5k MAS removed majority of the ^{1}H-^{1}H dipolar coupling in kerogen, suggesting kerogen has certain degree of internal molecular motion. Otherwise, it requires much higher MAS rate to achieve a significant reduction of homonuclear ^{1}H-^{1}H coupling. The results also suggest the 2.7 kHz linewidth at static state at 500 MHz for the remaining liquid in the kerogen sample is dominated by the bulk susceptibility effect from paramagnetic electron spins.

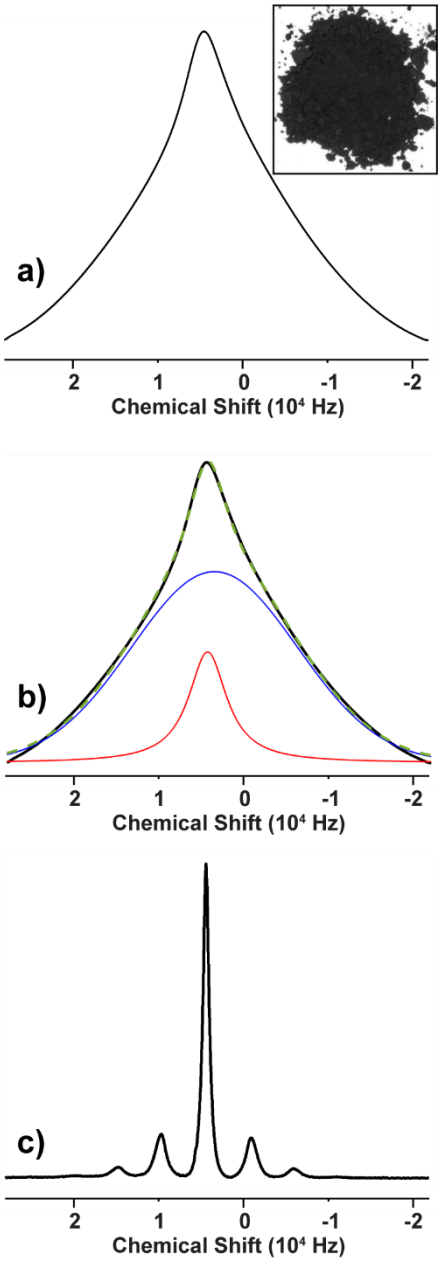

Fig. 4. a) Static ^{1}H NMR spectrum of dried isolated kerogen from source rocks acquired at 500 MHz with inset a photo of the isolated kerogen. b) decomposition of the acquired spectrum a) using one Gaussian (blue) and one Lorentzian (red) lines. c) ^{1}H spectrum of isolated kerogen at a MAS rate of 5 kHz.

3.2 2D T_1-T_2 spectrum of core plug

Fig. 5 shows a 2D T_1-T_2 NMR spectrum acquired on a preserved source rock plug saturated with Isopar using an inversion-recovery pulse sequence and echo time of 110 μs on a 12 MHz spectrometer [54]. Similar or more complex $2T_1T_{21}$-T_2 spectra have been widely reported and discussed [22, 24-34]. Almost all the reported T_2 T_1-T_2 spectra of source rocks in the laboratory or from the subsurface include peaks or a section of peaks with large T_1/T_2 ratios, more than 5, as indicated with the dashed red ellipse in **Fig. 5**.

Large T_1/T_2 ratio of nuclear spins are a typical property for solid state samples [38]. However, at 12 MHz NMR with the first data point acquired at 110 μs after the detection pulse, only the fluids in the source rocks can be observed. The observed peaks with large T_1/T_2 ratio in the 2D T_1-T_2 spectra was attributed to fluids in nanopores coupled by the intermolecular dipolar cross-relaxation with the solid kerogen matrix, thereby imparting NMR property similar of solid to the liquid [39]. However, to explain the results in this way, it requires the coupling of spins between the pore fluids and matrix solids in a time scale faster than or comparable with the T_2 relaxation time of the studied peaks, which are approximately 1 ms or shorter. Therefore, the dipolar cross-relaxation rate needs to be ~10^6 s^{-1}, which is extremely large. In the following two sections, we examine the dipolar cross-relaxation between a two spins system.

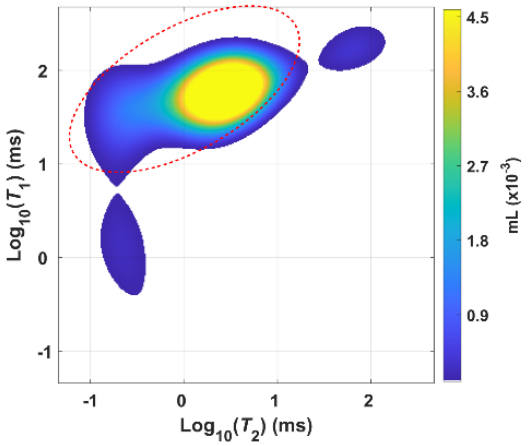

Fig. 5. An example 2D T_1-T_2 NMR spectrum of a saturated source rock plug. The dashed red ellipse shows a section of peaks with large T_1/T_2 ratio.

3.3 NMR signals of two group spins with cross-relaxation

Here, for simplicity, we only consider cross-relaxation of a two spin-group system comprising n_A magnetically equivalent spins in group A and n_B magnetically equivalent spins in group B. Both have spin quantum number $I = 1/2$. Note that n_A and n_B are number of spins in unit volume and thus represent the number density. The dipolar cross-relaxation between spin A and B are mutual, as

$$\boldsymbol{A} \underset{R_{BA}}{\overset{R_{AB}}{\rightleftharpoons}} \boldsymbol{B}. \tag{7}$$

The time dependent NMR magnetizations of a two spins system with auto- and cross-relaxation can be written as

$$\frac{d}{dt}\begin{bmatrix} M_z^A(t)-M_0^A \\ M_z^B(t)-M_0^B \end{bmatrix} = -\begin{bmatrix} R_{AA} & R_{AB} \\ R_{BA} & R_{BB} \end{bmatrix}\begin{bmatrix} M_z^A(0)-M_0^A \\ M_z^B(0)-M_0^B \end{bmatrix} \tag{8}$$

$$\frac{d}{dt}\begin{bmatrix} M_+^A(t) \\ M_+^B(t) \end{bmatrix} = -\begin{bmatrix} -i\omega_A + R_{AA} & R_{AB} \\ R_{BA} & -i\omega_A + R_{BB} \end{bmatrix}\begin{bmatrix} M_+^A(0) \\ M_+^B(0) \end{bmatrix} \tag{9}$$

With capital letter A and B in subscripts and superscripts representing corresponding group, M_Z longitudinal magnetization, M_0 equilibrium magnetization, $M_+ = M_x + iM_y$ transverse magnetization, and ω the chemical shift. The chemical shift term in the relaxation matrix for the transverse magnetization is important at high field; but is small and often can be neglected at very low field. Thus, at low field, the relaxation matrix is the same for transverse and longitudinal magnetizations. If we use $M_\delta^i(t) = M_z^i(t) - M_0^i$ ($i = A, B$), Eq. (8) and Eq. (9) can be written in the same form as

$$\frac{d}{dt}\begin{bmatrix} M_j^A(t) \\ M_j^B(t) \end{bmatrix} = -\begin{bmatrix} R_{AA} & R_{AB} \\ R_{BA} & R_{BB} \end{bmatrix}\begin{bmatrix} M_j^A(0) \\ M_j^B(0) \end{bmatrix} \tag{10}$$

with $j = \delta, +$.

Before we discuss each term in the relaxation matrix, the solution of Eq. (10) is

$$\begin{bmatrix} M_j^A(t) \\ M_j^B(t) \end{bmatrix} = \begin{bmatrix} a_{AA} & a_{AB} \\ a_{BA} & a_{BB} \end{bmatrix}\begin{bmatrix} M_j^A(0) \\ M_j^B(0) \end{bmatrix} \tag{11}$$

with

$$a_{AA}(t) = \frac{1}{2}\left[(1-\kappa)\exp(-\lambda_- t) + (1+\kappa)\exp(-\lambda_+ t)\right] \tag{12}$$

$$a_{BB}(t) = \frac{1}{2}\left[(1+\kappa)\exp(-\lambda_- t) + (1-\kappa)\exp(-\lambda_+ t)\right] \tag{13}$$

$$a_{AB}(t) = -\frac{R_{AB}}{\lambda_+ - \lambda_-}[\exp(-\lambda_- t) - \exp(-\lambda_+ t)] \tag{14}$$

$$a_{BA}(t) = -\frac{R_{BA}}{\lambda_+ - \lambda_-}[\exp(-\lambda_- t) - \exp(-\lambda_+ t)] \tag{15}$$

And

$$\kappa = \frac{R_{AA} - R_{BB}}{\lambda_+ - \lambda_-} \tag{16}$$

$$\lambda_\pm = \frac{1}{2}\{(R_{AA} + R_{BB}) \pm [(R_{AA} - R_{BB})^2 + 4R_{AB}R_{BA}]^{1/2}\} \tag{17}$$

Let's assume A and B represent hydrogen in pore fluids and the kerogen matrix, respectively. The NMR signals in any experiments can be evaluated using Eq. (11) with proper initial conditions setting up by the pulse sequence. For

example, considering spin *A* as the pore fluids and spin *B* as matrix solids, the detected NMR pore fluid signal in a CPMG experiment is

$$M_+^A(t) = a_{AA}M_0^A + a_{AB}M_0^B \tag{18}$$

with the initial condition $M_+^A(0) = M_0^A; M_+^B(0) = M_0^B$.

In an inversion recovery experiment, the longitudinal magnetizations for the pore fluid follows

$$M_z^A(t) = M_0^A - 2(a_{AA}M_0^A + a_{AB}M_0^B) \tag{19}$$

with the initial condition of both magnetizations of pore fluid and matrix solid spins inverted by the 180° pulse.

3.4 Intermolecular dipolar cross-relaxation

Here we only consider the cross-relaxation is intermolecular from translation diffusion in a low viscous solution. The relaxation rate in each term in the relaxation matrix in Eq. (10) can be expressed as [41, 45]

$$R_{AA} = n_A\rho_{AA} + n_B\rho_{BA} + R_A \tag{20}$$

$$R_{BB} = n_B\rho_{BB} + n_A\rho_{AB} + R_B \tag{21}$$

$$R_{AB} = n_A\rho_{AB}/2 \tag{22}$$

$$R_{BA} = n_B\rho_{BA}/2 \tag{23}$$

where ρ_{AA}, ρ_{BB}, ρ_{AB} and ρ_{BA} represent the relaxation rates of three possible pair of dipolar interaction *AA*, *BB*, and *AB*, respectively. R_A and R_B represent the external relaxation for the two nuclei, for example from intramolecular dipolar coupling and/or surface relaxation which are not examined here.

3.4.1 Intermolecular dipolar relaxation rate constant in bulk state

In bulk state, the normalized intermolecular dipolar relaxation rate constants are [41]

$$\rho_{AA} = \frac{c}{40}\frac{1}{D_{AA}\sigma_{AA}} \tag{24}$$

$$\rho_{BB} = \frac{c}{40}\frac{1}{D_{BB}\sigma_{BB}} \tag{25}$$

$$\rho_{AB} = \frac{c}{60}\frac{1}{D_{AB}\sigma_{AB}} \tag{26}$$

$$\rho_{BA} = \frac{c}{60}\frac{1}{D_{AB}\sigma_{AB}} \tag{27}$$

where $c = \mu_0^2\gamma_H^4\hbar^2/\pi$, $D_{AA} = 2D_A$, $D_{BB} = 2D_B$, and $D_{AB} = D_A + D_B$ are the mutual translational self-diffusion constants of the molecular pairs; σ_{AA}, σ_{BB}, σ_{AB} are the corresponding average closest internuclear distance.

Based on Eqs.(22), (23), (26), and (27), the cross-relaxation rates between the two spins are

$$R_{AB} = \frac{c}{120}\frac{n_A}{D_{AB}\sigma_{AB}}\ ;\ R_{BA} = \frac{c}{120}\frac{n_B}{D_{AB}\sigma_{AB}} \tag{28}$$

Note all the relaxation rates in Eq. (28) are at the magnitude of 10^{-3} s^{-1} in typical bulk solution. This is nine orders of magnitude smaller than the required 10^6 s^{-1} relaxation coupling between the fluid in nanopores and solid matrix to explain the peaks with large T_1/T_2 values in the ellipse in **Fig. 5**.

3.4.2 Dipolar cross-relaxation of nanoconfined liquid with solid

In a source rock sample, the fluids are confined in nanopores. Could this confinement enhance the cross-relaxation between liquid and solid to 10^6 s^{-1}? Source rock is too complicated to delineate this question. In this and subsequent sub-sections, we summarize the results on the intermolecular dipolar cross-relaxation between nanoconfined liquid and matrix solid using a synthetic uniform sample MCM41-C1 with a pore diameter of 2.57 nm on 500 MHz NMR (A detailed study was published in [58]).

Specifically, we measure and calculate the intermolecular cross-relaxation rate of protons of nanoconfined liquid CH_3OD and solid matrix MCM41-C1.

A schematic model of CH_3OD in a single MCM41-C1 pore is shown in **Fig. 6**a where the nucleus of interest, ^1H, is represented with white spheres. Note in MCM41-C1 the silica matrix is proton-free with the only protons appearing on the surface via methyl functional groups. The 1D proton MAS NMR spectrum of the CH_3OD saturated MCM41-C1 is shown in **Fig. 6**b. The peak at 3.31 ppm is the methyl proton of CH_3OD in the pore and the peak at 0.18 ppm is from the methyl proton on the MCM41-C1 pore surface. The linewidths at half height of the two peaks are 11 and 230 Hz, respectively. With MAS suppressing the net dipolar coupling of the solid protons and the magnetic field heterogeneity from local susceptibility for fluid protons [64], the peak linewidth is now determined by the transverse relaxation T_2. CH_3OD in the pore has a narrow linewidth because the molecular rotational motion is free. The translational motion of CH_3OD is aIso free in the time scale of $t \sim R^2/4D$, where R is the pore radius and D is the diffusion coefficient of CH_3OD. In contrast, the methyl protons on the MCM41-C1 surface are broader in linewidth due to the solid nature of the matrix, albeit they have some degree of free rotation along the carbon-silicon bond. Without MAS, the methyl proton of MCM41-C1 would be too broad to be detected.

Fig. 6c is a phase-sensitive 2D NOESY which is a fundamental NMR experiment for measuring cross-relaxation rates used in the determination of molecular structure [44, 45, 66]. The cross peaks represent the fraction of magnetization transfer from one spin to the other and thus depends on the cross-relaxation rate and sign. In the 2D NOESY spectra of **Fig.** 6c, the cross peaks between CH_3OD and MCM41-C1 are positive, which is the opposite result that would be generally

observed in a bulk solution where the cross peaks are negative from positive intermolecular cross-relaxation rates as shown in Eqs. (28) [45]. In addition, the cross peaks in **Fig. 6**c are strong in comparison to the diagonal peaks, in contrast to the generally weak cross peaks of intermolecular NOEs in bulk fluids with fast molecular tumbling [45, 51].

We used a selective NOE experiment [67, 68] to measure the intermolecular cross-relaxation rates between the methanol proton and solid methyl proton for higher accuracy than the 2D method. The selective pulse used was a 5 ms E-BURP-2 [57] and was on-resonance of the methanol methyl proton.

The signal intensity follows Eq. (11) with initial conditions $M_\delta^A(0) = -M_0^A$ and $M_\delta^B(0) = -2M_0^B$. The best fit to the experimental data was shown in **Fig. 6**d. The two curves were fit simultaneously with common parameters using a nonlinear regression method [69] and obtained the intermolecular cross-relaxation rate R_{BA} = -0.10±0.04 s^{-1}.

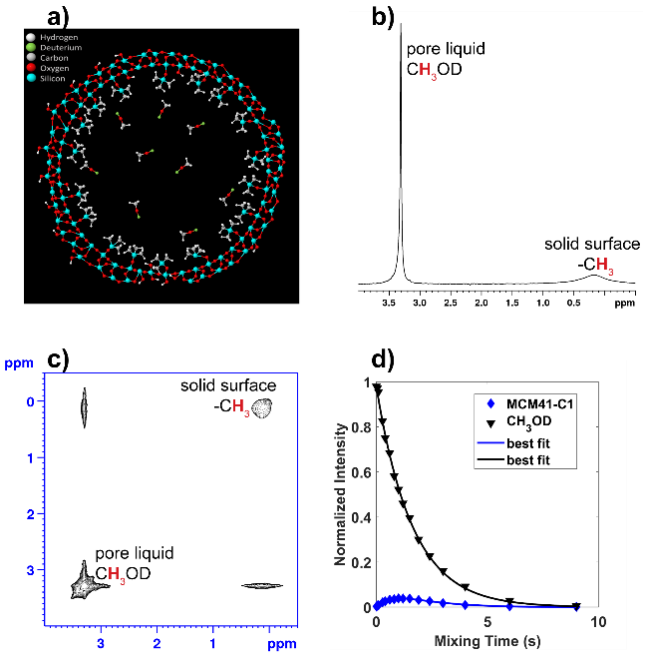

Fig. 6. NMR spectra of CH_3OD in methyl functionalized MCM41 (McM41-C1). a), schematic model of CH_3OD in MCM41-C1 with a diameter of 2.57 nm. b), 1D MAS NMR spectrum with the two peaks at 3.31 ppm and 0.18 ppm are the methyl protons of pore liquid methanol and solid surface MCM41-C1, respectively. c), 2D phase-sensitive NOESY spectrum with a mixing time 0.8 s. d), signal intensities at different mixing times from the selective-NOE experiments for the CH_3OD proton (triangles) and the MCM41-C1 proton (diamonds) with the best fit (curves) for the two-spin systems. The experiments were done at 22 °C.

3.4.3 Theoretical treatment of dipolar cross-relaxation of nanoconfined fluid with matrix solid

Without losing the generality and ease of comparison to experimental results, we only consider a two-dimensional (2D) pore with the assumption that the third dimension is infinitely long. Hence, in the third dimension, the intermolecular relaxation would be the same as in the bulk state.

When confined in a pore, a fluid molecule is reflected back into the pore cavity when it encounters the solid pore matrix. **Fig. 7** shows the simulated molecular diffusion of a fluid particle in two 2D circular pores of different radii: a), 50 nm and b), 2 nm. In (a), only a small section of the pore is shown. The blue-dot represents a fixed spin on the solid pore wall and the solid red-dot represents the initial position of the fluid spin, which is 0.3 nm from the fixed blue spin. The empty red-dot represent the final position of the moving spin. In the simulation, we used a diffusion coefficient of $D = 2\times10^{-9}$ m^2/s for the fluid molecule (It may be worthy to note here that although the molecular diffusion is the same in microscale, macroscopic diffusion coefficient in a nanopores measured by NMR would be different from this value because of the reflection by the pore wall). The solid straight lines represent 200 steps of a random-walk by diffusion of the fluid molecule within the pore. The diffusion process is random and thus **Fig. 7**a and 7b each represent only one scenario among infinite possibilities. It is evident, however, that the spin of a randomly diffusing molecule in a large pore, as illustrated in **Fig. 7**a, has a very small probability of being within 0.5 nm of the fixed red-spin again, as would be required for direct NMR dipolar relaxation. In contrast, the molecule in the smaller pore, which cannot escape the solid boundary, has a much greater probability of being less than 0.5 nm from the solid spin, as illustrated in **Fig. 7**b. As a result, the correlation of dipolar coupling between the fluid and solid spins is enhanced by the nanoconfinement.

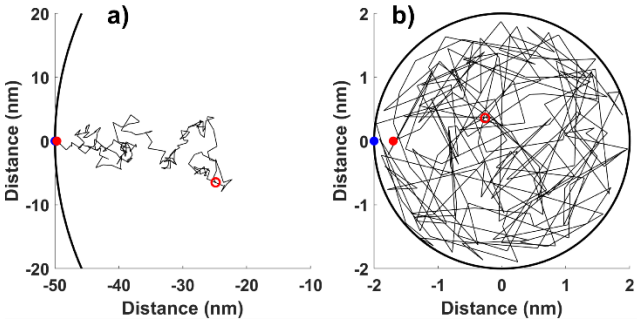

Fig. 7. The relative position of two spins from different molecules with one fixed on the pore surface (red dot) and the second one (black dot representing initial position) diffuses in a circular pore with radii of 50 nm (a) and 2.0 nm (b). The black line segments represent 200 step traces of diffusion that started at the same initial positions of 0.3 nm apart. The *x* and *y* components of each step were drawn from a normal distribution with a standard deviation of 0.9 nm, corresponding to a time step of 9 ps for a molecule with a diffusion coefficient $D = 2\times10^{-9}$ m^2/s based on the 2D Einstein-Smoluchowski relationship: $t = L^2 / 4D$.

The cross relaxation between nanoconfined liquid and solid matrix can be calculated in the 2D system, as [58]

$$R_{cr} = \frac{\mu_0^2\hbar^2\gamma^4 N\tau}{4\pi}\left(6\sum_{n=1}^{\infty}\frac{D_n^2}{V_{2n}}\frac{\beta_{2n}^2\tau}{\beta_{2n}^4+4\omega_0^2\tau^2}-\sum_{n=1}^{\infty}\frac{\tau C_n^2}{\beta_{0n}^2 V_{0n}}\right) \quad (29)$$

with

$$C_n = \frac{1}{2R} J_o'(\beta_{0n}\frac{\sigma}{2R})\Big[-Y_0(\beta_{0n})_1F_2(1;-\frac{1}{2},\frac{1}{2};-\frac{\beta_{0n}^2}{4}) + \beta_{0n}Y_1(\beta_{0n})_1F_2(1;\frac{1}{2},\frac{1}{2};-\frac{\beta_{0n}^2}{4}) + \frac{2R}{\sigma}Y_0(\beta_{0n}\frac{\sigma}{2R})_1F_2(1;-\frac{1}{2},\frac{1}{2};-\frac{\beta_{0n}^2}{4}\frac{\sigma^2}{4R^2}) - \beta_{0n}Y_1(\beta_{0n}\frac{\sigma}{2R})_1F_2(1;\frac{1}{2},\frac{1}{2};-\frac{\beta_{0n}^2}{4}\frac{\sigma^2}{4R^2})\Big] - \frac{1}{\sigma}Y_0'(\beta_{0n}\frac{\sigma}{2R})_1F_2(-\frac{1}{2};\frac{1}{2},1;-\frac{\beta_{0n}^2}{4}\frac{\sigma^2}{4R^2}) - \frac{1}{2R}Y_0'(\beta_{0n}\frac{\sigma}{2R})_1F_2(-\frac{1}{2};\frac{1}{2},1;-\frac{\beta_{0n}^2}{4}) \quad (30)$$

$$D_n = J_2'(\beta_{2n}\frac{\sigma}{2R})\left[\frac{1}{4R}G_{2,4}^{2,1}\left(\beta_{2n},\frac{1}{2}\middle|_{-1,1,-3/2,1/2}^{3/2,-3/2}\right) - \frac{1}{2a}G_{2,4}^{2,1}\left(\beta_{2n}\frac{\sigma}{2R},\frac{1}{2}\middle|_{-1,1,-3/2,1/2}^{3/2,-3/2}\right)\right] - Y_2'(\beta_{2n}\frac{\sigma}{2R})\left[\frac{1}{8}\frac{\beta_{2n}^2}{2R}\,{}_1F_2(\frac{1}{2};\frac{3}{2},3;-\frac{\beta_{2n}^2}{4}) - \frac{\sigma\beta_{2n}^2}{32R^2}\,{}_1F_2(\frac{1}{2};\frac{3}{2},3;-\frac{\sigma^2\beta_{2n}^2}{16R^2})\right] \quad (31)$$

where ${}_1F_2(a_1;\ b_1,\ b_2;\ x)$ is the generalized hypergeometric function and $G_{2,4}^{2,1}\left(x,y\middle|\begin{matrix}a_1,a_2\\b_1,b_2,b_3,b_4\end{matrix}\right)$ is the Meijer G-function[70] .

We evaluated Eq. (29) using Wolfram Mathematica 11.1 and plotted the cross-relaxation rate versus the closest distance of the fluid spin and spin on the pore surface σ in **Fig. 8**. The other parameters used were r = 1.3 nm, σ =1.8 Å, $N = 6.05 \times 10^{18}$ spins/m^2 for 2D number density, $D = 1.21 \times 10^{-9}$ m^2/s for the 2D diffusion coefficient which is 2/3 of the measured 3D diffusion coefficient at 22 °C. At 500 MHz, the theoretical rate is ~0.1 s^{-1} which is consistent with the experimentally measured value of CH_3OD and MCM41-C1. It should be noted that the simulation of molecular diffusion in 2D nanopores in **Fig. 7** and the theoretical calculations of Eq. (29) as in reference [58] did not require assumption of one or two layers of molecules on the pore surface exhibiting significant slower molecular motion. In our experiments, we utilized nanotubes with a diameter of 2.57 nm. The presence of one or two layers of slow motion molecules would constitute a substantial fraction of the total confined fluids, leading to a much larger intermolecular dipolar cross-relaxation than what was observed and calculated here.

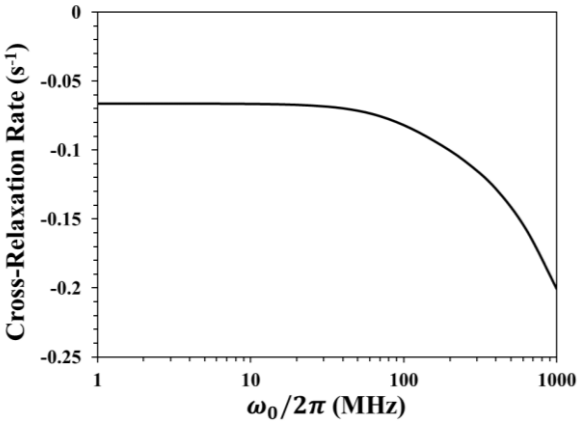

Fig. 8. Dipolar relaxation rate between nanoconfined fluids with solid matrix at different NMR frequency.

Both experiment and theory show that nanoconfinement enhances the cross-relaxation rate between the confined liquid and matrix solid by two orders of magnitude to 10^{-1} s^{-1} from the bulk state value 10^{-3} s^{-1}. However, even with the enhancement, it is still about 7 orders of magnitude too small to explain the large T_1/T_2 peaks in the ellipses in **Fig. 5** is by the dipolar cross-relaxation coupling which requires a rate about 10^6 s^{-1}.

3.5 Model for light hydrocarbon in source rocks

The pore diameter of the sample used in section 3.4 is only 2.57 nm. Further changing the pore size does not change the dipolar cross-relaxation rate between confined fluid and matrix solid significantly. We can conclude the observed large T_1/T_2 peaks in 2D T_1-T_2 spectra is not because the fluids coupled with the kerogen solid.

Instead, a viable interpretation to the observed large T_1/T_2 peaks in **Fig. 5** is that the motion of the fluid molecules is not free. This is an NMR manifestation of absorption of small hydrocarbon molecules into the kerogen matrix, as illustrated in a 2D scheme in **Fig. 9**. In **Fig. 9**, the black box represents the kerogen matrix and the empty spaces between kerogen represent a nanopore. In this model, small hydrocarbon molecules are in three different states: free in the pore bulk or pore interior, adsorbed on the pore surface, and absorbed in the kerogen matrix. **Fig. 9** depicts the pore fluids as in gas state where density of adsorbed gas is higher than that of pore bulk. The adsorbed molecules rapidly exchange with the molecules in the pore bulk. The residence time scale of individual adsorbed molecule on the surface is ps in the absence of chemical bond with the matrix. If the pore fluid is liquid, the density of adsorbed portion is similar to that of the pore bulk.

In the schematic model of **Fig. 9**, absorbed hydrocarbon molecules in kerogen retain a certain degree of motion so that it cannot be considered a solid, which would have too short of a T_2 that cannot be measured, as discussed in section 3.1.

It should be noted that the absorption of large amounts of light hydrocarbon in the kerogen matrix has long been suggested [71, 72]. However, direct experimental verification has not been reported until recently [73], likely because of the complexity and heterogeneity of the source rock matrix and the enclosed fluids. The 2D T_1-T_2 NMR spectra may, for the first time, be able to provide an experimental method to quantify the absorbed hydrocarbon in kerogen matrix of source rocks by integration of the peak volumes with large T_1/T_2 values in the spectra.

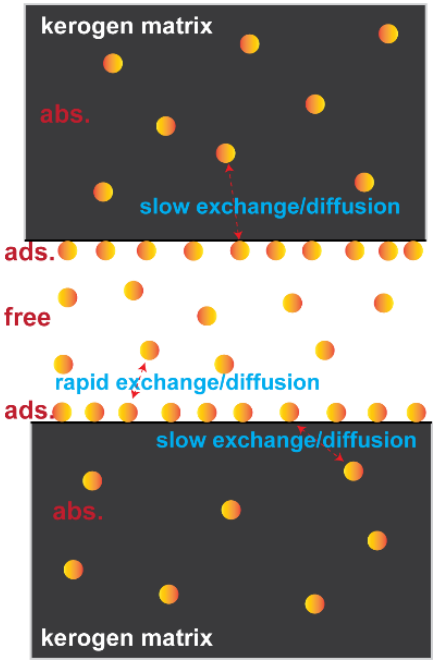

Fig. 9. Illustration of hydrocarbon storage model based on the NMR T_1-T_2 2D NMR and analysis of dipolar proton-proton dipolar interaction and relaxation.

4 Conclusion

We examined and discussed the impact of the molecular motion to the observed NMR results in source rocks at low and high fields.

For solid kerogen, the acquired NMR proton spectrum, with a linewidth at half height of 13.8 kHz, is dominated by proton dipolar coupling. It was determined that kerogen solid cannot be acquired by regular low field NMR instruments when the first data point is acquired at about 100 μs after the excitation because of the rapid decay of NMR signal by this large dipolar interaction. On this type of NMR instrument with long pre-scan delays, the detected signals are all from fluids.

We also re-examined the applicability of NMR relaxation theory developed for bulk state to nanoconfined fluids. It was found, both theoretically and experimentally, the nanoconfinement leads to an increase in the intermolecular dipolar cross-relaxation rate by two orders of magnitude.

We further concluded that even with the significant enhancement from nanoconfinement, the dipolar cross-relaxation between the pore fluid and kerogen matrix remains too small to explain the observed peaks with large T_1/T_2 ratio in 2D T_1-T_2 spectra. We suggested that these peaks are from absorbed hydrocarbons in the kerogen matrix in source rocks.

5 Reference

1. K.J. Dunn, D.J. Bergman, and G.A. LaTorraca, *Nuclear Magnetic Resonance: Petrophysical and Logging Applications*. (Elsevier Science. 2002).
2. R.J.S. Brown and I. Fatt. in *Fall Meeting of the Petroleum Branch of AIME.* (1956)
3. R.J.S. Brown and B.W. Gamson. 1960, Society of Petroleum Engineers. p. 9.
4. D.E. Woessner. in *Encyclopedia of Nuclear Magnetic Resonance* Vol. 1 (ed D.M.G.a.R.K. Harris) 700 (John Wiley & Sons, 1996).
5. J.J. Howard, W.E. Kenyon, and C. Straley, SPE Form Eval, **8**, 194–200 (1993)
6. M.N. Miller, et al. in *SPE Annual Technical Conference and Exhibition.* New Orleans, Louisiana (1990)
7. R.L. Kleinberg, W.E. Kenyon, and P.P. Mitra, J. Magn. Reson. A, **108**, 206-214 (1994)
8. D.T. Georgi and S. Chen. in *Offshore Mediterranean Conference and Exhibition.* (2007)
9. M. Appel, et al. in *SPWLA 41st Annual Logging Symposium.* Dallas, Texas, USA (2000)
10. W.E. Kenyon, The Log Analyst, 21-43 (1997)
11. R.G. Loucks, et al., AAPG Bulletin, **96**, 1071-1098 (2012)
12. R.G. Loucks, et al., J. Sediment. Res., **79**, 848-861 (2009)
13. D.L. Turcotte, E.M. Moores, and J.B. Rundle, Physics Today, **67**, 34-39 (2014)
14. M. Vandenbroucke and C. Largeau, Organic Geochemistry, **38**, 719-833 (2007)
15. B.M. Krooss, et al., Chemical Geology, **126**, 291-318 (1995)
16. A. Orangi, et al. in *SPE Hydraulic Fracturing Technology Conference.* (2011)
17. R.G. Loucks, et al., Journal of Sedimentary Research, **79**, 848-861 (2009)
18. M.M. Labani, et al., Journal of Petroleum Science and Engineering, **112**, 7-16 (2013)
19. S. Chen, et al. in *SPWLA 54th Annual Logging Symposium.* New Orleans, Louisiana (2013)
20. B. Sun;, et al. in *SPWLA 57th Annual Logging Symposium.* Reykjavik, Iceland (2016)
21. J.-H. Chen, S. Althaus, and M. Boudjatit. in *SPE/AAPG/SEG Unconventional Resources Technology Conference.* (2021)
22. Y.-Q. Song and R. Kausik, Progress in Nuclear Magnetic Resonance Spectroscopy, **112-113**, 17-33 (2019)
23. J.-H. Chen, M. Boudjatit, and S.M. Althaus. in *Physics of Fluid Flow and Transport in Unconventional Reservoir Rocks* 113-137 (2023).
24. M. Fleury and M. Romero-Sarmiento, Journal of Petroleum Science and Engineering, **137**, 55-62 (2016)
25. S. Khatibi, et al., International Journal of Chemical Engineering and Applications, (2018)
26. D. Yang and R. Kausik, Energy & Fuels, **30**, 4509-4519 (2016)
27. J. Li, et al., Energy & Fuels, **32**, 9043-9054 (2018)
28. S. Khatibi, et al., Fuel, **235**, 167-177 (2019)
29. X. Zeng, et al., Energy & Fuels, **34**, 5599-5610 (2020)
30. J. Li, et al., Marine and Petroleum Geology, **116**, 104311 (2020)

31. P. Zhang, et al., Marine and Petroleum Geology, **114**, 104210 (2020)
32. G. Zhou, et al., Journal of Petroleum Science and Engineering, **195**, 107926 (2020)
33. F. Panattoni, et al., Energy & Fuels, **35**, 18194-18209 (2021)
34. W. Yan, et al., Fuel, **206**, 89-98 (2017)
35. B.C. Anger, et al. in *International Symposium of the Society of Core Analysts* Snowmass, Colorado, USA (2016)
36. B. NICOT, et al. in *the International Symposium of the Society of Core Analysts* St. John's Newfoundland and Labrador, Canada (2015)
37. M. Fleury. in *the International Symposium of the Society of Core Analysts.* Avignon, France (2014)
38. A. Abragam, *The Principles of Nuclear Magnetism*. (London: Clarendon Press. 1961).
39. K.E. Washburn and Y. Cheng, Journal of Magnetic Resonance, **278**, 18-24 (2017)
40. I. Solomon, Physical Review, **99**, 559-565 (1955)
41. J.H. Noggle and R.E. Schirmer, *The Nuclear Overhauser Effect. Chemical Applications*. (New York: Academic Press. 1971).
42. K. Wüthrich, *NMR of Proteins and Nucleic Acids*. (Wiley. 1986).
43. N. Bloembergen, E.M. Purcell, and R.V. Pound, Physical Review, **73**, 679-712 (1948)
44. J. Jeener, et al., J. Chem. Phys., **71**, 4546-4553 (1979)
45. S. Macura and R.R. Ernst, Molecular Physics, **41**, 95-117 (1980)
46. S. Forsén and R.A. Hoffman, J. Chem. Phys. , **39**, 2892–2901 (1963)
47. G.A. Morris and R. Freeman, J Magn Reson, **213**, 214-43 (1978)
48. H.Y. Carr and E.M. Purcell, Physical Review, **94**, 630-638 (1954)
49. S. Meiboom and D. Gill, Review of Scientific Instruments, **29**, 688-691 (1958)
50. S. Berger and S. Braun, *200 and More NMR Experiments: A Practical Course*. (Wiley. 2004).
51. J.-H. Chen, A. Haghmoradi, and S.M. Althaus, J. Phys. Chem. B, **124**, 10237-10244 (2020)
52. S. Althaus, et al. in *SPE/AAPG/SEG Unconventional Resources Technology Conference.* Denver, Colorado, USA (2019)
53. V. Bortolotti, et al., SoftwareX, **20**, 101240 (2022)
54. S. Althaus, et al. in *SPWLA 64th Annual Logging Symposium.* Lake Conroe, TX, USA (2023)
55. W.L.K. Thomson, Phil. Mag., **42**, 448-452 (1871)
56. E. Barsotti, et al., Fuel, **184**, 344-361 (2016)
57. H. Geen and R. Freeman, J. Magn. Reson., **93**, 93-141 (1991)
58. J.-H. Chen, et al., ACS Omega, **7**, 45189-45196 (2022)
59. M.H. Levitt, *Spin Dynamics: Basics of Nuclear Magnetic Resonance*. (Wiley. 2001).
60. G.E. Pake, The Journal of Chemical Physics, **16**, 327-336 (1948)
61. A. Bielecki and A. Pines, Journal of Magnetic Resonance, **74**, 381-385 (1987)
62. J.H. Van Vleck, Physical Review, **74**, 1168-1183 (1948)
63. H.C. Torrey, Physical Review, **92**, 962-969 (1953)
64. J.-H. Chen and S. Singer. in *The Handbook of Metabonomics and Metabolomics* (eds J.C. Lindon, J.K. Nicholson, and E. Holmes) 113-147 (Elsevier Science B.V., 2007).
65. M.M. Maricq and J.S. Waugh, The Journal of Chemical Physics, **70**, 3300-3316 (1979)
66. K. Wuthrich, Science, **243**, 45-50 (1989)
67. H. Kessler, et al., J. Magn. Reson., **70**, 106-133 (1986)
68. J.-H. Chen, et al., Magnetic Resonance in Medicine, **55**, 1246-1256 (2006)
69. C. Avinadav. 2016: MATLAB Central File Exchange.
70. E.W. Weisstein. *From MathWorld--A Wolfram Web Resource*. MathWorld--A Wolfram Web Resource.
71. E.I. Sandvik, W.A. Young, and D.J. Curry, Organic Geochemistry, **19**, 77-87 (1992)
72. S.R. Etminan, et al., International Journal of Coal Geology, **123**, 10-19 (2014)
73. B. Nicot, et al., Magn. Reson., **3**, 125-136 (2022)